Machine learning predicts the glass transition of two-dimensional colloids besides medium-range crystalline order

Eun Cheol Kim,* Dong Jae Chun,* Chung Bin Park, and Bong June Sung
Department of Chemistry, Sogang University, Seoul 04107, Republic of Korea

(Received 6 March 2023; accepted 10 August 2023; published 9 October 2023)

We employ only the positions of colloidal particles and construct machine learning (ML) models to test the presence of structural order in glass transition for two kinds of two-dimensional (2D) colloids: 2D *polydisperse* colloids (PC) with medium-range crystalline order (MRCO) and 2D *binary* colloids (BC) without MRCO. ML models predict the glass transition of 2D colloids successfully without any information on MRCO. Even certain ML models trained with BC predict the glass transition of PC successfully, thus suggesting that universal structural characteristics would exist besides MRCO.

DOI: 10.1103/PhysRevE.108.044602

I. INTRODUCTION

Whether the glass transition relates to the structure of glasses is an open and challenging question [1–17], partly because a certain structural order correlates strongly with the dynamics of some glasses but fails to explain the dynamics of other types of glasses [18]. For example, in two-dimensional (2D) polydisperse colloids (PC), hexatic local structures grow quickly along with the dynamic correlation length (ξ_4) of PC [2,11], which is well known as the medium-range crystalline order (MRCO). MRCO has been, therefore, considered as structural order that might characterize the glass transition [12,17,19,20]. In 2D binary colloids (BC), however, any explicit local structure was not found to grow significantly near the glass transition [18]. This poses a question of whether there would be a universal structural order for two-dimensional glasses besides MRCO. We construct convolutional neural network (CNN) models by employing only the colloid positions from images of 2D colloids. The CNN models can distinguish the liquid and the glass states of colloids successfully. More interestingly, certain CNN models trained only with images of BC can predict the state of PC successfully without using information on MRCO. This indicates that there should be a universal structure that characterizes the 2D glass transition.

When liquids are cooled quickly toward the glass transition avoiding crystallization, the viscosity increases by orders of magnitude with no apparent structural change [21–24]. The dynamics of glasses become not only slow but also spatially heterogeneous, thus breaking the fluctuation-dissipation theorem [2,5,10,17,25–27]. Such slow and heterogeneous dynamics of glasses can be observed in various systems including colloidal suspensions, gels, porous materials, and biological cells [5,19,28–31]. The structure of glasses is not very different from that of liquids such that the radial distribution functions, the second-order spatial correlation of particles, cannot tell the difference between liquids and glasses, for which the structure-property relationship breaks down for the glassy dynamics [32]. The identification of structural order that characterizes the glass transition and dynamics has been, therefore, an issue of study [4,6,7,12,15,16,28,33].

2D colloidal systems have served as excellent testbeds to investigate the structural order in glasses, because the positions of colloidal particles could be tracked readily in both experiments and simulations [10,17–19,28,32,33]. 2D colloids also exhibit rich structures depending on the size distribution of colloidal particles. When one prepares PC with the Gaussian size distribution of colloids, local hexatic structures develop near the glass transition and their correlation length (ξ_6) diverges near the glass transition along with the dynamic correlation length (ξ_4) [2,11,19,20]. On the other hand, the hexatic local structure develops only weakly for BC such that the hexatic order and MRCO do not account for the divergence of ξ_4 near the glass transition [13,18,20,34–36]. Recently, Tong and Tanaka introduced a structural order parameter that measures the deviation of the local packing from optimized configuration, which accounts for the slow dynamics of both PC and BC successfully [13]. The relevance of structural order to the glass dynamics is still highly system dependent [8], thus becoming a hurdle to understanding the glass transition.

Machine learning (ML) methods have been employed extensively to search for the structural order in glasses [16,37–45]. Bapst *et al.* reported graph neural networks that could determine the long-time evolution of particles solely from initial particle positions of Kob-Andersen (KA) liquids [43]. Swanson *et al.* showed that CNN models and message passing neural networks could classify liquid and glass states of 2D KA liquids successfully [44]. Since they trained deep learning models with only particle positions (rudimentary structural information), the success of those models indicates that there should exist a structural order that can characterize the glass transition. Inspired by the work of Swanson *et al.* [44], we construct CNN models with images of either PC or BC. We employ CNN models trained with BC images to test and predict PC. And we also employ CNN models trained with PC images to predict BC. This allows us to test whether MRCO is a structural predictor to characterize the glass transition of PC and whether there would be a universal structural order for 2D colloids.

*These authors contributed equally to this work.

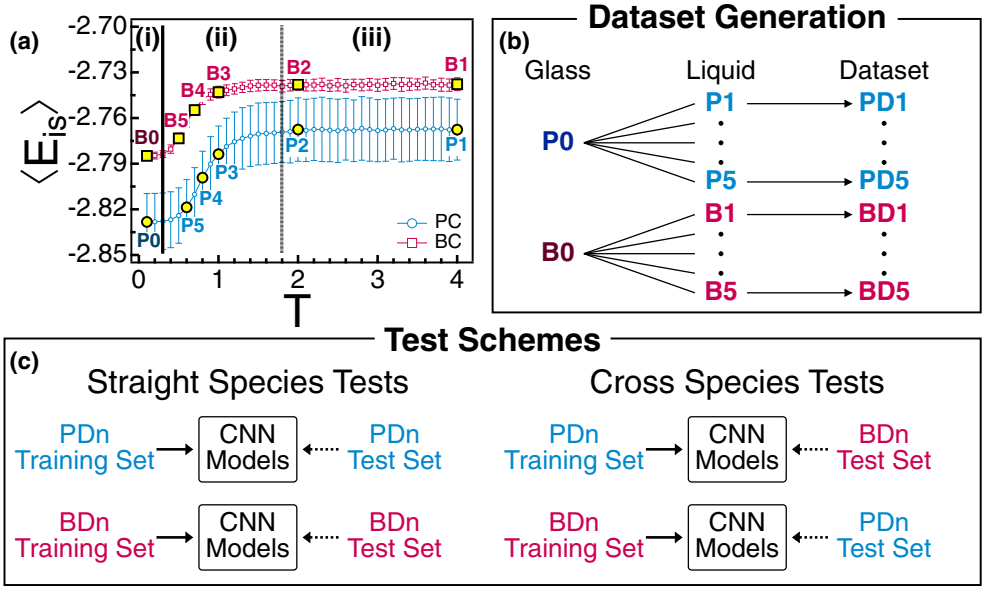

FIG. 1. (a) Inherent structure energies ($\langle E_{is} \rangle$) of PC (blue circles) and BC (red squares) as a function of T. The graph is divided into three regimes: (i) glass, (ii) supercooled liquid, and (iii) simple liquid. One glass, three supercooled liquids, and two simple liquids are selected to generate datasets. All the systems are cooled with a given cooling rate $\Gamma = 3.33 \times 10^{-4}$. (b) Each dataset contains images of 10 000 glass configurations (either P0 for PC or B0 for BC) and 10 000 liquid configurations (Pn for PC or Bn for BC with $n = 1$ to 5). (c) Test schemes in this study. In straight species tests (SSTs), CNN models trained with PDn (BDn) train sets are tested with PDn (BDn) test sets. In cross species tests (CSTs), CNN models trained with PDn (BDn) train sets are tested with BDn (PDn) test sets.

II. MODEL AND METHODS

We perform molecular dynamics simulations to generate configurations of PC and BC in both liquid and glass states using LAMMPS (large-scale atomic-molecular massively parallel simulator) package [46–48]. In the case of PC, we sample the diameter (σ_i) of the ith disk from the Gaussian distribution, which is generated using a Box-Muller transform method. The average diameter ($\langle \sigma_i \rangle$) of disks of PC is set to 1σ, which is the unit of length in this study. The polydispersity $\Delta \equiv \frac{\sqrt{\langle \sigma_i^2 \rangle - \langle \sigma_i \rangle^2}}{\langle \sigma_i \rangle}$ of PC, defined as the relative standard deviation of σ_i, is 0.11. BC consists of equal numbers of large and small disks of diameters, σ_L and σ_S, respectively. The size ratio $\Lambda \equiv \sigma_L/\sigma_S = 1.4$, with $\sigma_L = 1.16\sigma$ and $\sigma_S = 0.83\sigma$ for BC. For both PC and BC, we do not observe any liquid-to-hexatic phase transition and confirm that the glassy dynamics in this simulation appears at sufficiently low temperatures.

The total number (N) of disks is 3578 and the size of the systems (L) is 61.18σ for both PC and BC such that the area fraction $\phi \equiv \sum_{i=1}^{N} (\pi \sigma_i^2/4L^2)$ and the number density $\rho \equiv N/L^2$ are 0.76 and $0.956\sigma^{-2}$, respectively, for all systems in this study. Disks interact with each other via truncated and shifted Lennard-Jones potential $U(r)$ as follows:

$$U(r) = \begin{cases} U_{LJ}(r) - U_{LJ}(r_{\rm cut}), & r < r_{\rm cut}, \\ 0, & r \geqslant r_{\rm cut}, \end{cases} \quad (1)$$

where $U_{LJ}(r) = 4\varepsilon[(\sigma_{ij}/r)^{12} - (\sigma_{ij}/r)^6]$, $\varepsilon = 1k_BT$, $r_{\rm cut} = 2.5\sigma_{ij}$, and $\sigma_{ij} = (\sigma_i + \sigma_j)/2$. The mass ($m_i$) of the ith disk is set proportional to the area of the disk, $m_i \equiv \sigma_i^2$. The unit of mass is that of the disk of $\sigma_i = 1\sigma$. k_BT and $\tau = \sqrt{m\sigma^2/k_BT}$ are the units of energy and time, respectively, where k_B is the Boltzmann constant. We perform simulations under the canonical NVT ensemble condition with the velocity-Verlet integrator and Nosé-Hoover thermostat. The integration time step is set to 0.0025τ.

We prepare 10 000 independent initial configurations for PC and 10 000 for BC by placing the disks randomly in a square box with periodic boundary conditions and sampling the initial velocities randomly from the Maxwell-Boltzmann distribution at $T = 4$. All of the initial configurations are equilibrated until the kinetic and potential energies converge. After the equilibration at $T = 4$, each system is cooled down from $T = 4$ to $T = 0.1$ with a given cooling rate $\Gamma = 3.33 \times 10^{-4}$. Here, 10 000 configurations are used to generate liquid configurations at various temperatures and the 10 000 configurations are used to generate glass configurations at $T = 0.1$, which is below the glass transition temperature (T_g).

We calculate the average inherent structure energy ($\langle E_{is} \rangle$) at each temperature by minimizing the energies of given systems [Fig. 1(a)]. We identify the states of systems based on $\langle E_{is} \rangle$: glass, supercooled liquid, and simple liquid [1,23,49]. The glass transition temperatures (T_g's) of PC and BC are about $T_g = 0.4$ and 0.3. We determine the value of T_g from the inherent structure energy ($\langle E_{is} \rangle$) by identifying the point of two linear regimes of $\langle E_{is} \rangle$: one for supercooled liquid and another for glass [44,49–51]. We choose five representative liquid systems as indicated in Fig. 1(a) including two simple [(B1, B2) and (P1, P2)] and three supercooled liquid states [(B3, B4, B5) and (P3, P4, P5)]. Then, we pair 10 000 configurations of glasses (B0 or P0) with 10 000 configurations of one liquid state to make one dataset [Fig. 1(b)]. We prepare five datasets for PC, which we call PD1 to PD5 in the order of

decreasing temperature of liquids. Similarly, we also prepare five datasets for BC from BD1 to BD5.

We use the Python TensorFlow package [52] to construct CNN ML models, which carry out binary classifications into glass and liquid states. In order to let our CNN models carry out binary classifications with prepared datasets above, each configuration in the datasets is rendered as a 250 px × 250 px grayscale PNG image snapshot. We have 3578 white dots using only the (x, y) coordinates of the disks in a black background. Note that the sizes of dots are equal in both PC and BC snapshots such that CNN models perform binary classifications without any information about the size distributions or disparities of particles in a configuration. We split each dataset (from PD1 to PD5 and from BD1 to BD5) into train set (60%), validation set (20%), and test set (20%).

Our CNN models contain four two-dimensional convolution layers with 32, 64, 128, and 128 filters, respectively. Each convolution layer has a 3 × 3 kernel window with stride of 1, which can be considered as an eye of CNN models, and activated by ReLU activation function. A two-dimensional max pooling operation layer that has a 2 × 2 pooling window with strides of 2 is affixed to each convolution layer such that the feature maps are downsampled by a factor of 2. A dropout layer with the rate of 0.5, followed by a dense layer with 512 nodes and ReLU activation function, is added after four successive convolution layers. As a classifier, another dense layer with only one node is appended and activated by the sigmoid function. In our CNN models, binary cross entropy and RMSprop optimizer with learning rate 0.0001 are employed as a loss function and an optimizer, respectively.

We use the area under the receiver operating characteristic curve (AUC-ROC) values to evaluate the performance of CNN models. In order to calculate the AUC-ROC value of each CNN model, we first draw the receiver operating characteristic (ROC) curve by (i) calculating the false positive rate (*FPR*, also known as fallout, the ratio of "incorrectly classified" negative data to all negative data) and the true positive rate (*TPR*, also known as sensitivity, the ratio of "correctly classified" positive data) of the CNN model and (ii) plotting *FPR* versus *TPR* by switching the classification threshold from zero to one. In this study, "positive" data are equivalent to "glass" configurations and "negative" data are equivalent to "liquid" configurations. When the classifier successfully classifies the data, the ROC graph goes upper left (which corresponds to *low FPR* and *high TPR*) and would have the area value of unity. On the other hand, when the classifier completely fails to classify the data, the ROC graph goes straight from (0,0) to (1,1) (which corresponds to *high FPR* or *low TPR*) and would have the area value of 0.5. AUC-ROC value of each CNN model in this study is computed by employing *keras.metrics.AUC* class from Python Keras API [53] and the *num_thresholds* argument of 20 000.

We perform two different types of tests for our CNN models: (1) *straight species tests* (SSTs) and (2) *cross species tests* (CSTs) [Fig. 1(c)]. In the case of SSTs, the colloidal types of train and test datasets are identical. For instance, CNN models trained with PC train datasets (PD1–PD5) are used to predict the states of PC test datasets. In the case of CSTs, on the other hand, train and test datasets are different. For example, CNN models trained with BC train datasets (BD1–BD5) are employed to predict the states of PC test datasets.

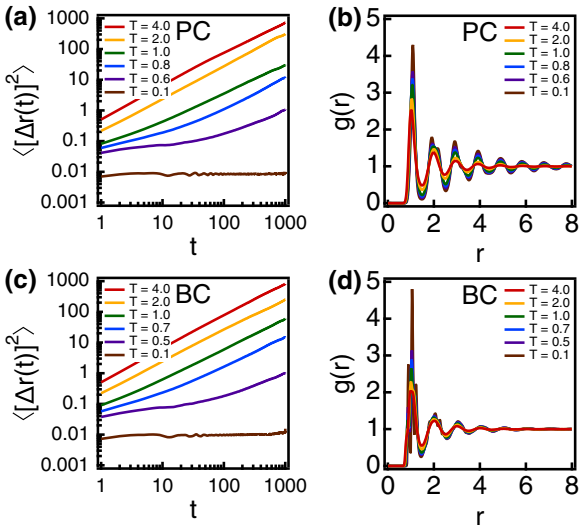

FIG. 2. Mean square displacements $\langle[\Delta r(t)]^2\rangle$ and radial distribution functions $g(r)$ of (a),(b) PC and (c),(d) BC at given temperatures.

III. RESULTS AND DISCUSSIONS

A. Transport and structural properties of PC and BC

As the temperature decreases, the colloid diffusion of both PC and BC slows down significantly, while their structures [characterized by the radial distribution function $g(r)$] do not change much. Figures 2(a)–2(d) depict the mean square displacements $\langle[\Delta r(t)]^2\rangle$ of colloid particles and $g(r)$ of PC and BC at different temperatures. At high temperatures, $\langle[\Delta r(t)]^2\rangle \sim t^1$ such that both PC and BC exhibit Fickian diffusion. For supercooled liquids (for example, at $T = 0.6$ for PC and $T = 0.5$ for BC), the subdiffusive regimes appear in $\langle[\Delta r(t)]^2\rangle$. For glass states at $T = 0.1$ for both PC and BC, however, particles do not diffuse in our simulation timescales. While particles do not diffuse and their viscosities increase tremendously, long-range correlations are not observed in $g(r)$ even at $T = 0.1$, thus implying that PC and BC are amorphous. The peaks of $g(r)$ in BC are sharper than those in PC, which indicates that PC and BC would have different local structures.

PC glasses exhibit medium-range crystalline order clearly while BC glasses do not. We calculate the local hexatic order parameter ($|\psi_6^j|$) of each colloidal particle by using $\psi_6^j = (1/N_j)\sum_{k=1}^{N_j} \exp(6i\theta_{jk})$, where N_j is the number of adjacent particles and θ_{jk} denotes the angle between a vector from the jth disk to its kth neighbor disk and an arbitrary reference vector. Figures 3(a) and 3(b) depict representative snapshots of PC and BC glasses, respectively, where the color code represents the value of $|\psi_6^j|$. In PC glasses [Fig. 3(a)], the yellow particles with $|\psi_6^j| \approx 1$, which maintain highly hexatic orders, gather together and construct highly crystalline domains. On the other hand, in BC glasses [Fig. 3(b)], the yellow particles are scattered throughout the simulation system.

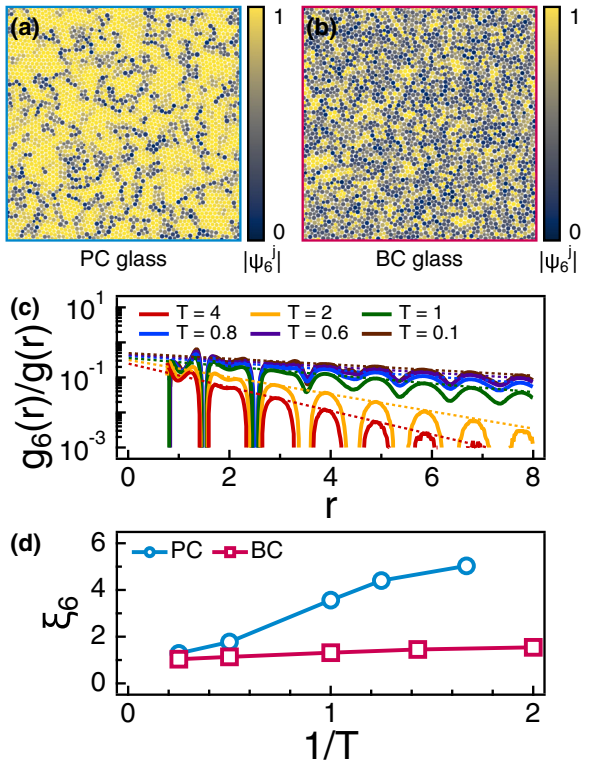

FIG. 3. Representative snapshots of the MRCO map of (a) PC glass and (b) BC glass. The color code of the disks represents the value of the local hexatic order parameter ($|\psi_6^j|$). (c) The hexatic order correlation functions [$g_6(r)$] of PCs divided by their radial distribution function [$g(r)$] at the selected temperatures. The peaks of the graph decay exponentially when the system is in the isotropic fluid phase. (d) The hexatic order correlation length (ξ_6) of PC liquids (blue circles) and BC liquids (red squares).

We estimate the hexatic order correlation length (ξ_6) by calculating the hexatic order correlation function [$g_6(r) \equiv \langle \psi_6^{i*}(r)\psi_6^j(0)\rangle$] [Fig. 3(c)]. In the case of the isotropic fluid phase, $g_6(r)$ is expected to decay exponentially, i.e., $g_6(r) \sim \exp(-r/\xi_6)$, and ξ_6 is considered as the characteristic size of MRCO of the system. Figure 3(c) depicts $g_6(r)$ divided by the radial distribution function [$g(r)$], where the peaks in $g_6(r)/g(r)$ decay exponentially. As T decreases down to T_g, ξ_6 of PC diverges quickly while that of BC does not increase rapidly, which is consistent with previous studies [11,18] [Fig. 3(d)].

B. Straight species tests of CNN ML models

We calculate the AUC-ROC values to evaluate the performance of our CNN models. AUC-ROC values have been used to evaluate the performance of the classification problem for ML [44,54]. When AUC-ROC $\approx$ 1, we may regard the CNN model as a successful one that can predict whether the system corresponds to either glass or liquid.

In the case of straight species tests (SSTs), where CNN models trained with PC (BC) training data are employed to predict the glass transition of PC (BC), most of the AUC-ROC values are close to 1 for both PC and BC. This indicates that our CNN models predict the glass transition of 2D colloids

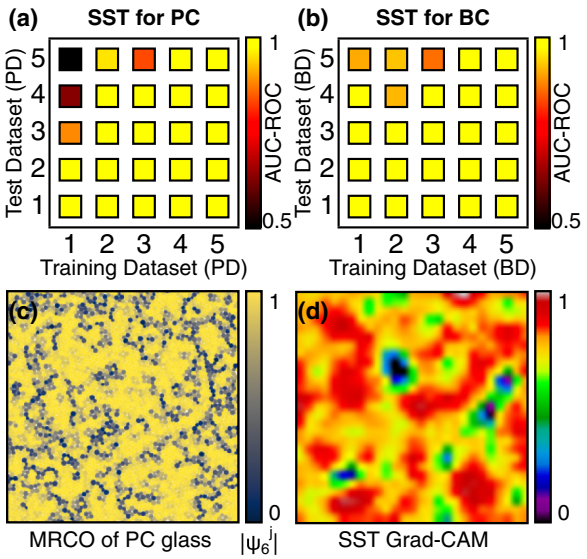

FIG. 4. AUC-ROC values of the straight species tests (SSTs) for (a) PC and (b) BC. (c) The MRCO image and (d) the SST Grad-CAM image of one identical representative PC glass configuration.

quite successfully. Figures 4(a) and 4(b) depict the AUC-ROC values for various cases of SSTs. For example, AUC-ROC $\approx$1 with a yellow box at (PD5, PD1) in Fig. 4(a). This is when a CNN model is trained with the train dataset PD5 and is employed to predict the test dataset PD1. This indicates that, when a CNN model is constructed by using the configurations of PC glasses and PC supercooled liquids (PD5), the CNN model tells the difference successfully between PC glasses and PC liquids at a relatively high temperature (PD1). Because CNN models are trained with only structural information (the positions of colloids), the success of SSTs indicates that CNN models can take advantage of structural characteristic for the classification successfully. This also suggests that there could be a structural order, which enables the CNN model to characterize the glass transition.

When CNN models are trained using configurations of glasses and high temperature liquids, the CNN models fail to classify the glasses and the low temperature supercooled liquids [the upper left corners of Figs. 4(a) and 4(b)]. This is because the CNN models are forced to learn the features of the high temperature liquids. Then, the CNN models may not capture the difference between supercooled liquids and glasses relatively well.

When our CNN models try to predict the glass transition, they consider a more complex structural pattern rather than MRCO. We employ the Grad-CAM (gradient-weighted class activation mapping) algorithm [55] to interpret how CNN models tell the difference between liquid and glass states. The image of Grad-CAM allows us to investigate which region of the image is being used for the CNN model to make a prediction. Grad-CAM results of CNN models are constructed via the following steps. First, we identify the last convolutional layer, which is the convolutional layer with 128 filters in this study. Second, we calculate the neuron importance weight $\alpha_k^C = \frac{1}{uv}\sum_i^u \sum_j^v \frac{\partial y^C}{\partial A_{ij}^k}$ of the kth feature map of the last

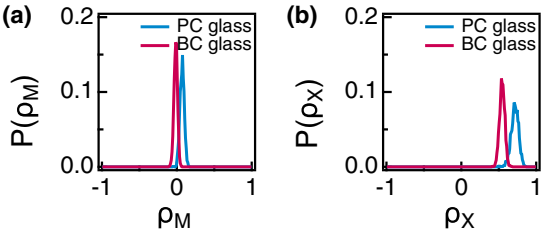

FIG. 5. (a) Distribution functions $[P(\rho_M)]$ of the correlation coefficients (ρ_M) between the MRCO images and the SST Grad-CAM images for PC and BC glass configurations. (b) The distribution functions $[P(\rho_X)]$ of the correlation coefficients (ρ_X) between the SST Grad-CAM images and the CST Grad-CAM images for PC and BC glass configurations.

convolutional layer. Here, y^C is the score for class C (which is composed of two elements, glass and liquid), A^k_{ij} is the (i, j) component of the kth feature map, and u and v are the width and the height of the kth feature map, respectively. A^k_{ij} is the (i, j) component of the kth feature map. Finally, we compute the ReLU score of linear combination of the weights and the corresponding feature map $L^C = \mathrm{ReLU}(\sum_k \alpha^C_k A^k_{ij}) = \max(0, \sum_k \alpha^C_k A^k_{ij})$ and make a heat map image using this ReLU score. Figures 4(c) and 4(d) depict the representative images of MRCO and Grad-CAM of the identical glass configuration of PC. The MRCO domain with high hexatic order $(|\psi^j_6|)$ does not correspond to the region of the image that the CNN model considers critical.

In order to calculate the correlation between MRCO and the structure that our CNN models consider critical, we convert MRCO and Grad-CAM images, which are generated during SSTs for all the glass configurations in the test dataset, into grayscale figures. Also, we compute the correlation coefficients (ρ_M) between them by comparing the brightness of each pixel [Fig. 5(a)]. For the fair comparison, we resize the Grad-CAM images to the size of MRCO images by using the bilinear interpolation method. If the MRCO domain were to correspond to the region highlighted in the Grad-CAM image, $\rho_M \approx -1$. As shown in Fig. 5(a), $\rho_M \approx 0$ for both PC and BC glasses, thus indicating that CNN models do not employ MRCO but predict the glass transition of both PC and BC glasses successfully.

C. Cross species tests of CNN ML models

We also perform cross species tests (CSTs), i.e., we train a CNN model with a BC train set and utilize the CNN model to predict the glass transition of a PC test set, and vice versa. Figures 6(a) and 6(b) depict the performance (AUC-ROC) of CSTs of CNN models. Not surprisingly, the performance of CNN models for CSTs is not as good as for SSTs. However, when CNN models are trained with BC glasses and supercooled liquids (BD5 train set), the CNN model can predict the glass transition of PC quite successfully except for the PD5 test set. Similarly, when CNN models are trained with PC glasses and high temperature liquids (PD1 train set), the CNN model can predict the glass transition of all BC test sets successfully.

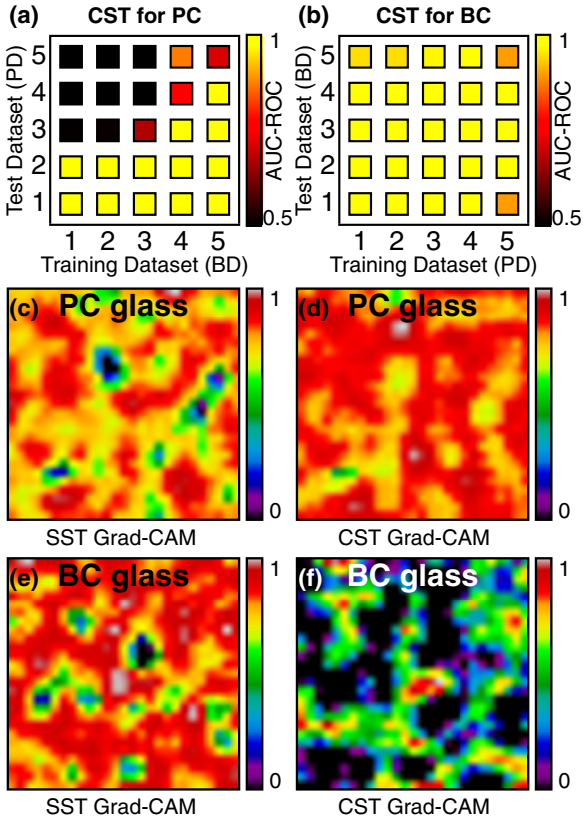

FIG. 6. AUC-ROC values of the cross species tests (CSTs) for (a) PCs and (b) BCs. (c) The SST Grad-CAM image and (d) CST Grad-CAM image of an identical representative PC glass configuration. (e) The SST Grad-CAM image and (f) CST Grad-CAM image of an identical representative BC glass configuration.

Considering (i) that PC glasses do own MRCO domains but BC glasses do not and (ii) that a certain CNN model trained with BC glasses still may predict the glass transition of PC, MRCO would not be the structural information that CNN models take advantage of for the prediction. More interestingly, CNN models trained with BC are likely to utilize structural information similar to what CNN models trained with PC consider important. Figures 6(c) and 6(d) depict the Grad-CAM images that CNN models trained with PC and BC test sets produced while predicting the glass state of the identical PC glass configuration. The highlighted regions of Fig. 6(c) correspond to those of Fig. 6(d). Similarly, Figs. 6(e) and 6(f) show the Grad-CAM images of an identical BC glass configuration generated by CNN models trained with BC and PC, respectively. Note that both CNN models highlight similar regions.

We calculate the correlation coefficients (ρ_X) between Grad-CAM images generated by CNN models trained with PD1 and BD1 for all the glass configurations [Fig. 5(b)]. ρ_X quantifies how much similar structural information would be used by CNN models trained with PC and BC when predicting the states of identical glass configurations. Figure 5(b) depicts the values of ρ_X for the predictions of BC (red) and PC (blue) glasses. $\rho_X \approx 0.52$ and 0.7 for BC and PC glasses, respectively, thus indicating that the structural

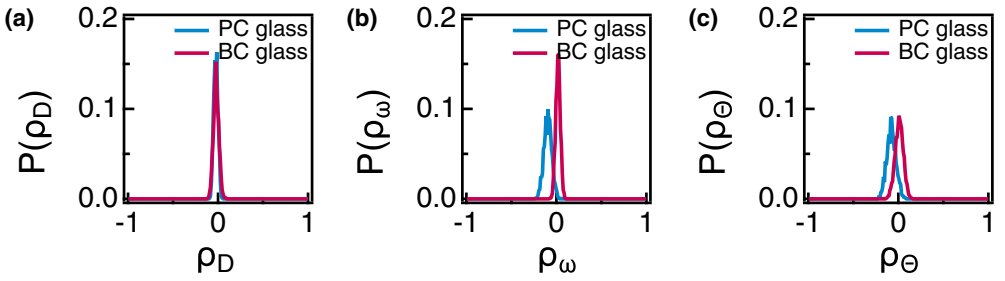

FIG. 7. (a) Distribution functions $[P(\rho_D)]$ of the correlation coefficients (ρ_D) between the local density images and the SST Grad-CAM images for PC and BC glass configurations. (b) The distribution functions $[P(\rho_\omega)]$ of the correlation coefficients (ρ_ω) between the images of the local disordered parameters and the SST Grad-CAM images for PC and BC glass configurations. (c) The distribution functions $[P(\rho_\Theta)]$ of the correlation coefficients (ρ_Θ) between the images of Tong-Tanaka steric favorability order parameters and the SST Grad-CAM images for PC and BC glass configurations.

information captured by CNN models trained with PC is correlated strongly with the structural information captured by CNN models trained with BC. In other words, the structural information obtained from BC glasses during training can be still utilized to predict the glass transition of PC. This also suggests that there should be a universal structural information in 2D colloids besides MRCO.

In order to find any structural characteristics that correlate with what our CNN models consider significant, we estimate the local number density, the local disorderedness parameter derived from hexatic order parameter [17], and the Tong-Tanaka steric favorability order parameter [13]. In order to calculate Pearson correlation coefficients between those parameters and Grad-CAM images, we divide our system into 27×27 lattices and count the particle number of each lattice. We normalize the local parameters by the particle number in the local lattice and generate 27 px $\times$ 27 px grayscale PNG images for those local parameters. Each pixel of the image has the normalized brightness value (0 for black and 1 for white) of the normalized local parameter.

Grad-CAM images that our CNN models produce during SSTs do not correlate any of those local parameters that we consider in this study. Figure 7 depicts the probability distribution functions $[P(\rho_D)$, $P(\rho_\omega)$, and $P(\rho_\Theta)]$ of correlations between local parameters [the local density (D), the local disordered parameter (ω), and the Tong-Tanaka steric favorability order parameter (Θ)] and the Grad-CAM images for both PC and BC glass configurations. All of those distribution functions are peaked at zero such that what our CNN models capture from glass configurations does not correlate with those local parameters.

It is of academic importance to understand whether the glass transition relates to the structural glasses and whether there would be a universal structure that characterizes the glass transition. Our study with CNN models suggests that there would be a universal structural characteristic besides MRCO, especially when predicting the glass transitions of 2D glasses. Unfortunately, however, in this study we cannot identify the salient (universal) structure that our CNN models take advantage of. We investigate local parameters such as the local density, the local disordered parameter, and the Tong-Tanaka steric favorability order parameter. But we find that they do not correlate with the Grad-CAM images produced by our CNN models. In our future study, we plan to extend our study and investigate Kob-Andersen and Wahnström systems. We plan to investigate whether the structural information used for CNN models in this study can be still applied to those systems.

IV. SUMMARY AND CONCLUSIONS

In this study, we introduce CNN ML models that we train with positions of colloids obtained from molecular dynamics simulations for PC and BC. The CNN models predict the states of 2D colloids in the straight species tests (SSTs) successfully, where CNN models trained with PC (BC) are employed to predict the states of PC (BC). This indicates that there should be structural characteristics that ML models can employ to predict the glass transition of 2D colloids. Also, certain CNN models perform well even in cross species tests (CSTs), where CNN models trained with BC (PC) are employed to predict the states of PC (BC). We also find that CNN models trained with either PC or BC consider similar regions of 2D colloids when trying to predict the states of the 2D colloids. This indicates that even though PC glasses do have a medium-range crystalline order (MRCO) but BC glasses do not, ML models may still capture a universal structural characteristic in 2D colloids besides MRCO.

ACKNOWLEDGMENTS

This work was supported by a National Research Foundation of Korea (NRF) grant funded by the Korea government (MSIT) (Grant No. 2019R1A2C2084053). This research was also supported by the Basic Science Research Program through the National Research Foundation of Korea (NRF) funded by the Ministry of Education (Grant No. 2018R1A6A1A03024940).

[1] S. Sastry, P. G. Debenedetti, and F. H. Stillinger, Nature (London) **393**, 554 (1998).

[2] T. Kawasaki, T. Araki, and H. Tanaka, Phys. Rev. Lett. **99**, 215701 (2007).

[3] M. Mosayebi, E. Del Gado, P. Ilg, and H. C. Öttinger, Phys. Rev. Lett. **104**, 205704 (2010).

[4] R. Candelier, A. Widmer-Cooper, J. K. Kummerfeld, O. Dauchot, G. Biroli, P. Harrowell, and D. R. Reichman, Phys. Rev. Lett. **105**, 135702 (2010).

[5] L. Berthier and G. Biroli, Rev. Mod. Phys. **83**, 587 (2011).

[6] M. Leocmach and H. Tanaka, Nat. Commun. **3**, 974 (2012).

[7] A. Malins, J. Eggers, C. P. Royall, S. R. Williams, and H. Tanaka, J. Chem. Phys. **138**, 12A535 (2013).

[8] G. M. Hocky, D. Coslovich, A. Ikeda, and D. R. Reichman, Phys. Rev. Lett. **113**, 157801 (2014).

[9] J. Kim and B. J. Sung, J. Chem. Phys. **141**, 014502 (2014).

[10] J. Kim and B. J. Sung, Phys. Rev. Lett. **115**, 158302 (2015).

[11] J. Russo and H. Tanaka, Proc. Natl. Acad. Sci. USA **112**, 6920 (2015).

[12] I. Tah, S. Sengupta, S. Sastry, C. Dasgupta, and S. Karmakar, Phys. Rev. Lett. **121**, 085703 (2018).

[13] H. Tong and H. Tanaka, Phys. Rev. X **8**, 011041 (2018).

[14] L. Berthier, M. Ozawa, and C. Scalliet, J. Chem. Phys. **150**, 160902 (2019).

[15] H. Tanaka, H. Tong, R. Shi, and J. Russo, Nat. Rev. Phys. **1**, 333 (2019).

[16] E. Boattini, S. Marín-Aguilar, S. Mitra, G. Foffi, F. Smallenburg, and L. Filion, Nat. Commun. **11**, 5479 (2020).

[17] D. J. Chun, Y. Oh, and B. J. Sung, Phys. Rev. E **104**, 054615 (2021).

[18] T. Kawasaki and H. Tanaka, J. Phys.: Condens. Matter **23**, 194121 (2011).

[19] K. Watanabe and H. Tanaka, Phys. Rev. Lett. **100**, 158002 (2008).

[20] H. Tanaka, T. Kawasaki, H. Shintani, and K. Watanabe, Nat. Mater. **9**, 324 (2010).

[21] G. S. Fulcher, J. Am. Ceram. Soc. **8**, 339 (1925).

[22] E. R. Weeks, J. C. Crocker, A. C. Levitt, A. Schofield, and D. A. Weitz, Science **287**, 627 (2000).

[23] P. G. Debenedetti and F. H. Stillinger, Nature (London) **410**, 259 (2001).

[24] J. C. Mauro, Y. Yue, A. J. Ellison, P. K. Gupta, and D. C. Allan, Proc. Natl. Acad. Sci. USA **106**, 19780 (2009).

[25] J. Kim and B. J. Sung, J. Phys.: Condens. Matter **27**, 235102 (2015).

[26] Y. Park, J. Kim, and B. J. Sung, J. Chem. Phys. **147**, 124503 (2017).

[27] S. Kwon, H. W. Cho, J. Kim, and B. J. Sung, Phys. Rev. Lett. **119**, 087801 (2017).

[28] C. P. Royall, S. R. Williams, T. Ohtsuka, and H. Tanaka, Nat. Mater. **7**, 556 (2008).

[29] W. K. Kipnusu, M. Elsayed, R. Krause-Rehberg, and F. Kremer, J. Chem. Phys. **146**, 203302 (2017).

[30] J. Hwang, J. Kim, and B. J. Sung, Phys. Rev. E **94**, 022614 (2016).

[31] B. R. Parry, I. V. Surovtsev, M. T. Cabeen, C. S. O'Hern, E. R. Dufresne, and C. Jacobs-Wagner, Cell **156**, 183 (2014).

[32] J. Kim, C. Kim, and B. J. Sung, Phys. Rev. Lett. **110**, 047801 (2013).

[33] X. Yang, R. Liu, M. Yang, W.-H. Wang, and K. Chen, Phys. Rev. Lett. **116**, 238003 (2016).

[34] R. D. Mountain and D. Thirumalai, Phys. Rev. A **36**, 3300 (1987).

[35] R. M. Ernst, S. R. Nagel, and G. S. Grest, Phys. Rev. B **43**, 8070 (1991).

[36] H. Tanaka, Eur. Phys. J. E **35**, 113 (2012).

[37] P. Geiger and C. Dellago, J. Chem. Phys. **139**, 164105 (2013).

[38] E. D. Cubuk, S. S. Schoenholz, J. M. Rieser, B. D. Malone, J. Rottler, D. J. Durian, E. Kaxiras, and A. J. Liu, Phys. Rev. Lett. **114**, 108001 (2015).

[39] E. D. Cubuk, S. S. Schoenholz, E. Kaxiras, and A. J. Liu, J. Phys. Chem. B **120**, 6139 (2016).

[40] C. Dietz, T. Kretz, and M. H. Thoma, Phys. Rev. E **96**, 011301(R) (2017).

[41] A. Ziletti, D. Kumar, M. Scheffler, and L. M. Ghiringhelli, Nat. Commun. **9**, 2775 (2018).

[42] D. Dai, Q. Liu, R. Hu, X. Wei, G. Ding, B. Xu, T. Xu, J. Zhang, Y. Xu, and H. Zhang, Mater. Des. **196**, 109194 (2020).

[43] V. Bapst, T. Keck, A. Grabska-Barwińska, C. Donner, E. D. Cubuk, S. S. Schoenholz, A. Obika, A. W. R. Nelson, T. Back, D. Hassabis, and P. Kohli, Nat. Phys. **16**, 448 (2020).

[44] K. Swanson, S. Trivedi, J. Lequieu, K. Swanson, and R. Kondor, Soft Matter **16**, 435 (2020).

[45] Z. Fan and E. Ma, Nat. Commun. **12**, 1506 (2021).

[46] https://www.lammps.org

[47] S. Plimpton, J. Comput. Phys. **117**, 1 (1995).

[48] A. P. Thompson, H. M. Aktulga, R. Berger, D. S. Bolintineanu, W. M. Brown, P. S. Crozier, P. J. in 't Veld, A. Kohlmeyer, S. G. Moore, T. D. Nguyen, R. Shan, M. J. Stevens, J. Tranchida, C. Trott, and S. J. Plimpton, Comput. Phys. Commun. **271**, 108171 (2022).

[49] J. Helfferich, I. Lyubimov, D. Reid, and J. J. de Pablo, Soft Matter **12**, 5898 (2016).

[50] H. Tong and H. Tanaka, Nat. Commun. **10**, 5596 (2019).

[51] N. Oyama, S. Koyama, and T. Kawasaki, Front. Phys. **10**, 1007861 (2023).

[52] M. Abadi, A. Agarwal, P. Barham, E. Brevdo, Z. Chen, C. Citro, G. S. Corrado, A. Davis, J. Dean, M. Devin, S. Ghemawat, I. Goodfellow, A. Harp, G. Irving, M. Isard, Y. Jia, R. Jozefowicz, L. Kaiser, M. Kudlur, J. Levenberg *et al.*, arXiv:1603.04467.

[53] https://keras.io.

[54] Z. Huang, J. Wu, and F. Xie, Mater. Lett. **293**, 129707 (2021).

[55] R. R. Selvaraju, M. Cogswell, A. Das, R. Vedantam, D. Parikh, and D. Batra, Int. J. Comput. Vis. **128**, 336 (2020).